Proceedings of the Seventh International Conference on
Railway Technology: Research, Development and Maintenance
Edited by: J. Pombo
Civil-Comp Conferences, Volume 15, Paper 23.8
Civil-Comp Press, Edinburgh, United Kingdom, 2026
ISSN: 2753-3239, doi: 10.4203/ccc.15.23.8

A Trackside Magnetic Field Energy Harvester: Coupled Modelling, Load Matching, and Energy Estimation from Train-Passage Measurements

C. Zuo and Y. Kuang

School of Civil Engineering, Central South University, Changsha, China

Abstract

An H-shaped magnetic field energy harvester was investigated for converting the alternating field generated by railway traction return current into electrical energy. A finite element model coupled to an external circuit was used to determine the equivalent impedance, tuning capacitance, matched load, and output response. At 50 Hz, the equivalent inductance and resistance were 18.4 H and 430 Ω, corresponding to a tuning capacitance of 550.66 nF and a matched load of 430 Ω. With a rail current amplitude of 300 A, the maximum average power and voltage amplitude across the load reached 763 mW and 25.6 V. Field measurements over 14 h 29 min 31 s recorded 140 train passages. The current in one rail was reconstructed from the measured magnetic flux density and used to estimate the temporal power profile. A representative interval of 3317 s containing 12 passages yielded 5.81 J at the load, whereas the complete campaign yielded 48.95 J. Sustained responses at moderate power contributed more energy than brief high power peaks, demonstrating that both output magnitude and duration are required to assess railway energy harvesters.

Keywords: energy harvesting, railway monitoring, magnetic field, traction return current, finite element modelling, field measurement, accumulated energy.

1 Introduction

The growing use of condition monitoring systems in railway infrastructure has led to the widespread deployment of distributed trackside sensors for measuring rail temperature, vibration, displacement, and structural condition [1]. These nodes are commonly installed over long distances and in harsh or difficult-to-access locations. Supplying them by cable entails substantial construction and wiring costs, whereas battery operation is constrained by limited battery life and periodic replacement [2]. Harvesting energy already present in the railway environment therefore offers an attractive route towards the autonomous operation of low-power monitoring equipment.

On electrified railways, traction current returns to the substation through the running rails and associated return conductors, creating an alternating magnetic field around each rail. A magnetic core and induction coil can convert part of this field energy into electricity [3]. Unlike harvesting from vibration, solar radiation, or thermal gradients, magnetic-field harvesting requires no direct mechanical coupling to the track, introduces little interference with train operation, and is largely independent of weather conditions [4]. Existing studies have concentrated on harvester topology [5], optimisation of the magnetic-flux path [6], and performance under prescribed current excitation [7]. Much less attention has been paid to quantifying the energy available during real train passages using field measurements. To address this gap, the present study develops a trackside magnetic-field energy harvester (MFEH) and a coupled electromagnetic-circuit model, examines the effects of rail current and load resistance, and establishes a quantitative relationship between rail current and maximum average output power. Magnetic-flux-density measurements collected during train passages are then used to reconstruct the current in a single rail, from which time-varying power and accumulated energy are estimated under actual operating conditions.

2 Trackside Magnetic Field Energy Harvester and Methodology

This section describes the harvester configuration, the coupled numerical model, and the procedure used to process the field measurements.

2.1 Configuration and operating principle

Figure 1 illustrates the proposed MFEH and its intended trackside location. The device is mounted beside the rail web, between adjacent fastening assemblies, where it can exploit the alternating field generated by traction-return current without encroaching on the vehicle kinematic envelope. With a plan-view envelope of approximately 300 mm × 108 mm, the unit fits around existing track components such as fasteners and sleepers, thereby limiting interference with the track structure and normal railway operation.

The MFEH consists of an H-shaped magnetic core and a 5000-turn induction coil. Two end limbs extend parallel to the rail, while a central limb forms the magnetic connection between them and carries the coil. The end limbs guide the surrounding alternating flux towards the central section. A minimum clearance of 40 mm is maintained between the rail web surface and the nearest surface of the MFEH. This spacing represents a compromise among flux concentration, rail eddy-current loss, and practical installation requirements.

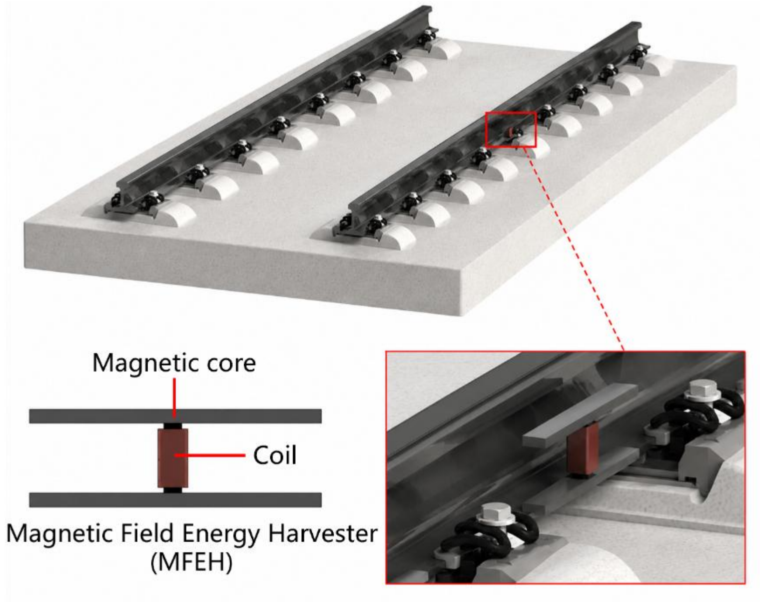

Figure 1: Configuration and trackside installation of the proposed MFEH.

During railway operation, traction return current generates a time-varying magnetic field around the rail [8]. The H-shaped core concentrates this field, causing the flux linked with the induction coil to vary periodically and inducing an open-circuit voltage U_{OC} in accordance with Faraday's law. Under sinusoidal steady state operation and within the linear magnetic regime, the voltage amplitude can be approximated as

$$EMF = U_{OC} = N\omega A_{c,e}\mu_{r,e}B_{ex} \tag{1}$$

where $\omega = 2\pi f$ is the angular frequency of the rail current, N is the number of coil turns, $A_{c,e}$ is the effective cross-sectional area of the central limb, $\mu_{r,e}$ is the effective relative permeability of the core, and B_{ex} denotes the mean external magnetic flux density over the central limb.

2.2 Equivalent circuit and coupled finite element model

With an external load connected, the MFEH may be represented by the series equivalent circuit in Figure 2(a). The source U_{OC} denotes the amplitude of the open-circuit voltage induced at the coil terminals. The combined effect of the coil and core is represented by the equivalent inductance L_{EH}, whereas R_{EH} accounts for winding resistance and core loss referred to the electrical side. A series capacitor C compensates the inductive reactance, and the useful output is taken as the average power dissipated in the load resistance R_L:

$$P = \frac{U_{OC}^2 \cdot R_L}{2\left[\left(R_{EH}+R_L\right)^2 + \left(\omega L_{EH} - \frac{1}{\omega C}\right)^2\right]} \tag{2}$$

For fixed U_{OC}, R_{EH}, L_{EH}, C, and ω, differentiating Equation (2) with respect to R_L shows that the maximum average power is obtained when the circuit is series-tuned and the resistances are matched, i.e. $C = 1/(\omega^2 L_{EH})$ and $R_L = R_{EH}$. The corresponding maximum average power is

$$P_{max} = \frac{U_{OC}^2}{8R_{EH}} = \frac{N^2\omega^2 A_{c,e}^2 \mu_{r,e}^2 B_{ex}^2}{8R_{EH}} \tag{3}$$

According to Equation (3), U_{OC} and R_{EH} directly determine the maximum average power, while L_{EH} enters through the capacitance required for resonance [9]. The equivalent parameters were extracted from the three-dimensional rail-MFEH-air model shown in Figure 2(b), and the principal inputs are listed in Table 1. The Magnetic and Electric Fields interface was solved in the frequency domain to describe induced currents and electromagnetic fields in conductive regions and to evaluate the complex coil terminal voltage and impedance. Chinese mainline AC electrified railways operate at the power frequency of 50 Hz [10], which was therefore adopted for the analysis. To determine the internal impedance, a 0.01 A sinusoidal test current was imposed on the coil and the resulting complex terminal voltage was evaluated. Their ratio gives the equivalent impedance Z, with Re(Z) = R_{EH} and Im(Z) = ωL_{EH}. The extracted parameters were then used to calculate the tuning capacitance and matched load at 50 Hz.

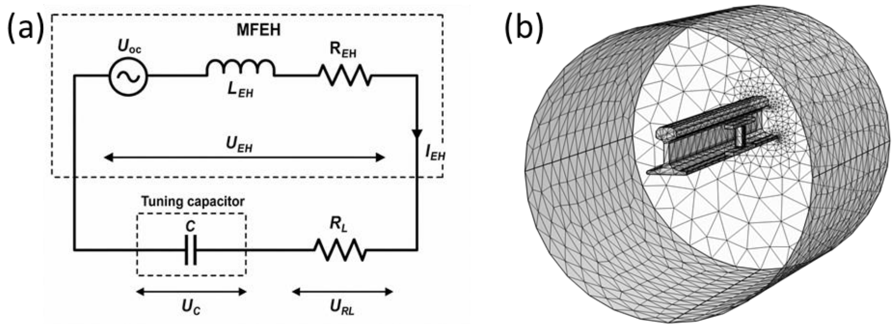

Figure 2: MFEH modelling: (a) series-tuned equivalent circuit, (b) finite element model and mesh.

To predict the MFEH output characteristics, the Circuit interface was coupled to the finite element model, with the coil terminals connected in series to C and R_L. A parameter sweep held I_{rail} at 300 A while varying R_L to verify the matching condition. The tuned capacitance and matched load were then fixed, and I_{rail} was swept over the prescribed range to obtain the load-voltage amplitude and average output power.

For subsequent conversion of field-reconstructed current into MFEH output power, the numerical data were approximated by a low-order polynomial subject to the physical constraints $P_{max}(0) = 0$ and $P_{max} \geq 0$:

$$P_{max} = \sum_{i=0}^{n} a_i \cdot I_{rail}^i \tag{4}$$

Here, a_i (i = 0, 1, …, n) denotes a fitting coefficient whose dimensions depend on the polynomial order. Within the linear magnetic regime, U_{OC} scales approximately with I_{rail}, while P_{max} scales with U_{OC}^2; a nearly quadratic dependence on I_{rail} is therefore expected. Accordingly, an origin-constrained quadratic model was adopted, with the fitted coefficient reported in Section 3.1.

Parameter	value	units
Central magnetic core dimensions	80 × 14 × 14	mm
End magnetic core dimensions	300 × 39 × 14	mm
Outer dimensions of coil	70 × 39 × 39	mm
Inner dimensions of coil	70×19×19	mm
Diameter of coil wire	0.35	mm
Number of coil turns	5000	-
Air domain dimensions	Φ500 × 1200	mm
Length of the rail	1200	mm
Lateral distance between MFEH and rail center planes	90	mm
Electrical conductivity(air)	1	S/m
Relative permeability(air)	1	-
Electrical conductivity(track)	3×10^6	S/m
Relative permeability(track)	30	-
Electrical conductivity(magnetic core)	1.2×10^4	S/m
Relative permeability(magnetic core)	3000	-

Table 1: Main parameters used in the finite element model.

2.3 Field measurement and data processing procedure

Field measurements were conducted at up-line chainage K190+101 on the Huainan Railway in Wuhu, Anhui Province, China, to characterise the time-varying magnetic field around the rail during actual train passages. As shown in Figure 3, an F901 triaxial magnetic-flux-density sensor (COLIY Technology GmbH) was mounted near the foot of the outer rail of the up line using a custom fixture and protective enclosure. The sensing centre was located 30 mm vertically from the rail foot surface and 66 mm horizontally from the longitudinal centre plane of the rail. Signals were digitised using an NI USB-9229 data acquisition device (NI (China) Instrument Co., Ltd.) at 5555.6 Hz and logged in real time using LabVIEW 2022 on a laptop.

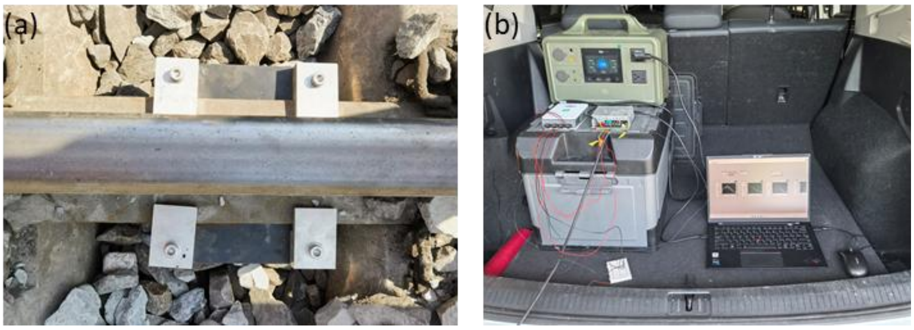

Figure 3: Field measurement system: (a) sensor installation, (b) data acquisition system.

Each channel was first de-meaned to remove its DC offset. A zero-phase 48-52 Hz Butterworth band-pass filter was then applied to retain the fundamental component associated with traction-return current while suppressing drift and out-of-band interference. The three filtered orthogonal components were combined vectorially. To preserve directional information, the sign of the resultant was assigned from the dominant component, yielding a signed equivalent 50 Hz magnetic-flux-density signal.

Calibration between the local magnetic field and the current in a single rail was obtained from the finite element model using the field sensor location. A series of current amplitudes was imposed on the rail, and the corresponding flux density at the measurement point was recorded. The resulting relationship was used to reconstruct I_{rail} from the field data. Equation (4) then provided the time-varying average power, and integration over the selected interval gave the accumulated energy:

$$E_m = \int_{t_1}^{t_2} P_{max}(t)dt \tag{5}$$

where t_1 and t_2 denote the beginning and end of the integration interval, respectively, and $P_{max}(t)$ is the time-varying average power predicted under tuned and matched-load conditions from the reconstructed rail current.

This procedure links measured magnetic field, reconstructed rail current, predicted output power, and accumulated energy, enabling the theoretical load-side energy available to the MFEH under actual railway operating conditions to be assessed.

3 Results and Discussion

The numerical and field results are presented in sequence, from magnetic response and load matching to rail current reconstruction and energy estimation.

3.1 Electromagnetic response and output characteristics

Figure 4 compares magnetic-flux-density contours around the rail cross-section at a rail current amplitude of 100 A, before and after installation of the MFEH. In the absence of the harvester, the contours form approximately closed loops around the rail and decay progressively with distance. At 50 Hz, the combined influence of rail geometry and current redistribution produces local concentrations near the corners of the rail head and foot, where the peak flux density is approximately 176 μT.

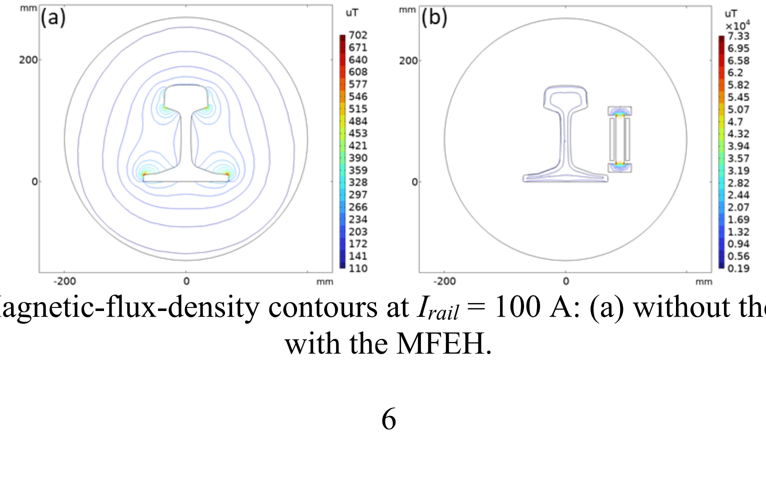

Figure 4: Magnetic-flux-density contours at I_{rail} = 100 A: (a) without the MFEH, (b) with the MFEH.

Introducing the MFEH reshapes the local field because the high-permeability core provides a low-reluctance path for the surrounding flux. The strongest concentration occurs in the end limbs nearest the rail, where the maximum flux density reaches 7.33 × 10^4 μT. This redistribution increases the flux linked with the induction coil. Because Figures 4(a) and 4(b) use different colour scales, quantitative comparison should be based on the reported numerical values rather than apparent colour intensity.

Applying the procedure described in Section 2.2, the equivalent inductance and resistance at 50 Hz were calculated as L_{EH} = 18.4 H and R_{EH} = 430 Ω, respectively, corresponding to a tuning capacitance of C = 550.66 nF. Figure 5(a) presents the average output power as a function of R_L for I_{rail} = 300 A. The power initially rises sharply with load resistance, reaches a maximum of 763 mW at R_L = 430 Ω, and then declines. This response agrees with the maximum-power-transfer condition for the series-tuned circuit. A very small load limits the load voltage, whereas an excessive load reduces circuit current. Matching R_L to R_{EH} provides the optimum balance. Accordingly, C = 550.66 nF and R_L = 430 Ω were retained for the subsequent current sweep.

Applying the procedure described in Section 2.2, the equivalent inductance and resistance at 50 Hz were calculated as L_{EH} = 18.4 H and R_{EH} = 430 Ω, respectively, corresponding to a tuning capacitance of C = 550.66 nF. Figure 5(a) presents the average output power as a function of R_L for I_{rail} = 300 A. The power initially rises sharply with load resistance, reaches a maximum of 763 mW at R_L = 430 Ω, and then declines. This response agrees with the maximum-power-transfer condition for the series-tuned circuit. A very small load limits the load voltage, whereas an excessive load reduces circuit current. Matching R_L to R_{EH} provides the optimum balance. Accordingly, C = 550.66 nF and R_L = 430 Ω were retained for the subsequent current sweep.

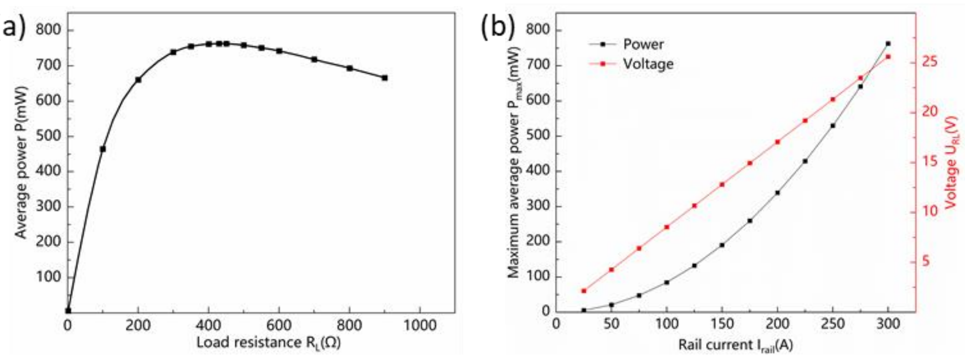

Figure 5: Simulated output characteristics: (a) average power versus R_L at I_{rail} = 300 A, (b) power and load voltage amplitude versus I_{rail}.

With C and R_L held constant, the parametric results in Figure 5(b) show that the load voltage amplitude U_{RL} increases almost linearly as I_{rail} rises from 25 to 300 A and reaches 25.6 V at 300 A. Over the same interval, P_{max} increases from 5.3 to 763 mW and follows an approximately quadratic trend. Provided that the core remains unsaturated, the external magnetic flux density scales approximately with I_{rail};

consequently, U_{OC} is proportional to I_{rail}, while P_{max} is proportional to U_{OC}^2. The observed dependence of P_{max} and I_{rail}^2 is thus physically consistent.

$$P_{max} = 8.47965397 \times 10^{-6} I_{rail}^2 \tag{6}$$

Applying the constraints $P_{max}(0) = 0$ and $P_{max} \geq 0$ gives the origin-constrained quadratic fit in Equation (6), where I_{rail} is expressed in amperes and P_{max} in watts. The coefficient of determination, $R^2 = 0.999999968$, confirms that the fitted function accurately represents the simulated response over 0–300 A and is suitable for converting reconstructed field currents into power and energy estimates.

3.2 Field measurements and rail-current reconstruction

The field campaign lasted 14 h 29 min 31 s and captured 140 train passages, comprising 75 on the up line and 65 on the down line. To illustrate the signal characteristics and processing procedure, a continuous 3317 s (55 min 17 s) segment was selected. During this interval, 12 trains passed the site, comprising five up-line and seven down-line movements.

The raw triaxial magnetic-flux-density signals are plotted in Figure 6(a). Between train passages, the three channels remain near their respective background levels, whereas each passage produces a distinct response in one or more components. Although the sensor was installed beside the outer rail of the up line, responses were also recorded when down-line trains passed, indicating that the local field is influenced by currents in the adjacent track and by the distribution of traction-return current among the rails and other return paths.

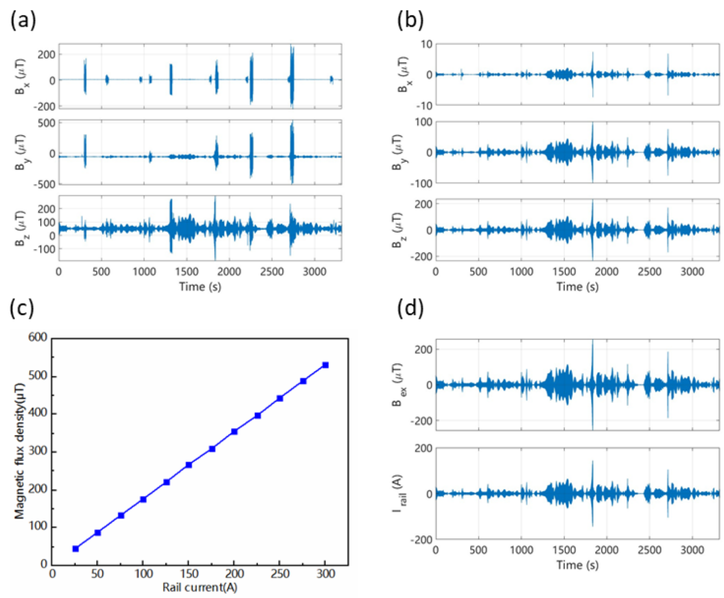

Figure 6: Field data processing and rail-current reconstruction: (a) raw three-axis flux-density signals, (b) filtered 50 Hz components, (c) B_{ex}-I_{rail} calibration, (d) signed resultant flux density and reconstructed rail current.

The raw data contain sensor offset, the static ambient field, low-frequency drift, and out-of-band components. After DC removal and 48–52 Hz band-pass filtering, the fundamental components shown in Figure 6(b) exhibit substantially reduced offsets and interference, making the train-related intervals more readily distinguishable.

To establish the field-to-current conversion, the field at the sensor location was calculated for a series of rail current amplitudes, as shown in Figure 6(c). Across 25–300 A, B_{ex} varies linearly with I_{rail}. An origin-constrained linear fit gives

$$B_{ex} = kI_{rail} \tag{7}$$

where $k = 1.77515 \times 10^{-6}$ T/A and $R^2 = 0.999999962$, demonstrating an excellent linear relationship between the flux density at the measurement point and the current in a single rail. The rail current can therefore be reconstructed as

$$I_{rail} = \frac{1}{k} B_{ex} \tag{8}$$

Figure 6(d) compares the signed resultant flux density with the reconstructed rail current. The maximum resultant flux density in the selected interval is 257.0 μT, corresponding to a peak rail current of 144.8 A. Both the peak magnitude and duration vary substantially between train passages. These differences may reflect running direction, train type, traction or braking state, and the distribution of return current between the two rails and the earthing system. Because neither train operating state nor rail current was measured simultaneously, the following analysis treats the continuous interval as the statistical unit and focuses on the combined effects of power magnitude, duration, and accumulated energy.

3.3 Train-passage power and energy assessment

Substituting the reconstructed current from Section 3.2 into Equation (6) yields the time-varying average output power over the selected 3317 s interval, as shown in Figure 7(a). The responses associated with individual train passages vary markedly in both peak magnitude and duration. Between approximately 1400 and 1600 s, for example, the power generally remains below 50 mW, yet the sustained moderate output increases the accumulated energy by about 1.56 J. By contrast, brief peaks of approximately 178 and 93 mW occur near 1835 and 2715 s, but contribute only about 0.77 and 0.22 J, respectively. The energy associated with a passage is therefore governed by the area under the power–time curve rather than by peak power alone.

The accumulated-energy trace in Figure 7(b) further illustrates this distinction. Short high-power events produce steep local rises, whereas lower-amplitude responses sustained over longer periods can deliver larger overall increments. The selected interval yields 5.81 J, of which the two principal peaks above 50 mW together account for approximately 0.99 J, or only 17% of the total. Performance assessment of a railway magnetic field energy harvester should therefore consider peak power, average power, effective duration, and accumulated energy together.

Across the complete 14 h 29 min 31 s campaign, the predicted theoretical load-side energy is 48.95 J, corresponding to a time-averaged power of approximately 0.94 mW; the selected 3317 s segment averages approximately 1.75 mW. For an energy-scale comparison, a 3.2 V, 600 mAh lithium iron phosphate cell stores approximately 6.91 kJ. If a comparable harvesting rate were available for 12 h per day, the MFEH would accumulate the same theoretical energy in approximately 170 days, before accounting for conversion and storage losses. This comparison is intended only to indicate energy scale; it does not imply direct battery charging or battery-equivalent continuous output. The available energy may nevertheless support intermittent, duty-cycled sensing and wireless transmission, subject to validation of the complete power management chain.

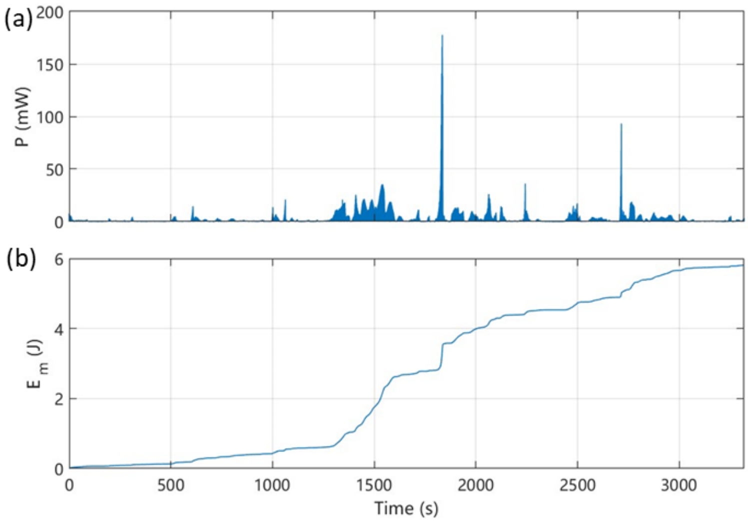

Figure 7: Predicted MFEH response over the selected 3317 s interval: (a) time-varying average output power, (b) accumulated load-side energy.

4 Conclusions

This study combined a coupled electromagnetic-circuit model with field magnetic measurements to assess the energy available to a trackside MFEH under actual train operation. The proposed framework reconstructs rail current from measured magnetic flux density and subsequently estimates time-varying average power and accumulated energy. The results indicate that the alternating field generated by traction return current constitutes a usable energy source and can be harvested without galvanic connection to the traction return circuit. The MFEH therefore has potential as a supplementary supply for low-power trackside monitoring nodes, reducing reliance on periodically replaced batteries.

Several limitations should nevertheless be recognised. The reported power and energy were inferred from field magnetic measurements, a finite element calibration, and a simulated power model; they have not yet been verified by direct electrical measurements from an MFEH prototype in service. The analysis also assumes ideal tuning and a matched resistive load and excludes losses in rectification, storage, voltage regulation, and power management. In addition, train type, operating state, and actual rail current were not measured concurrently, preventing the passage-to-passage variations from being attributed to individual operating factors.

Future work will therefore focus on prototype manufacture and long-term field trials with synchronous measurements of local magnetic field, rail current, and harvester terminal output. Rectification, energy storage, and ultra-low-power management circuitry will be incorporated into the system model and experimental platform. Extended datasets covering different lines, train types, and operating conditions will then be used to assess usable energy, supply reliability, and the practical suitability of the MFEH for duty-cycled wireless monitoring applications.

References

[1] V.J. Hodge, S. O'Keefe, M. Weeks, A. Moulds, "Wireless Sensor Networks for Condition Monitoring in the Railway Industry: A Survey", IEEE Transactions on Intelligent Transportation Systems, 16(3), 1088-1106, 2015.

[2] Y.L. Zhao, Z.Q. Liu, D. Yi, X.D. Yu, X.P. Sha, L.J. Li, H. Sun, Z.K. Zhan, W.J. Li, "A Review on Rail Defect Detection Systems Based on Wireless Sensors", Sensors, 22(17), 6409, 2022.

[3] A.E. Espe, T.S. Haugan, G. Mathisen, "Magnetic Field Energy Harvesting in Railway", IEEE Transactions on Power Electronics, 37(7), 8659-8668, 2022.

[4] J.Y. Zuo, L.W. Dong, F. Yang, Z.H. Guo, T.P. Wang, L. Zuo, "Energy Harvesting Solutions for Railway Transportation: A Comprehensive Review", Renewable Energy, 202, 56-87, 2023.

[5] H.Y. Yang, Y. Li, Z.W. Liu, H.J. Luo, Y.H. Yan, Z.Y. He, "An Accurate Power Model and High Power Density Design Method of Free-Standing Magnetic Field Energy Harvesters With H-Shaped Core", IEEE Transactions on Industrial Electronics, 70(8), 7965-7975, 2023.

[6] S. Yuan, Y. Huang, J. Zhou, Q. Xu, C. Song, G. Yuan, "A High-Efficiency Helical Core for Magnetic Field Energy Harvesting", IEEE Transactions on Power Electronics, 32(7), 5365-5376, 2017.

[7] S. Yuan, Y. Huang, J. Zhou, Q. Xu, C. Song, P. Thompson, "Magnetic Field Energy Harvesting Under Overhead Power Lines", IEEE Transactions on Power Electronics, 30(11), 6191-6202, 2015.

[8] Y. Kuang, Z.J. Chew, T.W. Ruan, T. Lane, B. Allen, B. Nayar, M.L. Zhu, "Magnetic Field Energy Harvesting from the Traction Return Current in Rail Tracks", Applied Energy, 292, 116911, 2021.

[9] Y. Kuang, C.C. Zuo, X.F. Gu, "Design, Modelling and Field Test of a Track-Borne Magnetic Field Energy Harvester for Electrified Railways", Applied Energy, 401, 126665, 2025.

[10] H.T. Hu, Y.J. Liu, Y. Li, Z.Y. He, S.B. Gao, X.J. Zhu, H.D. Tao, "Traction Power Systems for Electrified Railways: Evolution, State of the Art, and Future Trends", Railway Engineering Science, 32, 1-19, 2024.